Mechanical properties of bilayer WS_2 and Graphene-WS_2 Hybrid composites by molecular dynamics simulations

OPEN ACCESS
IOP Publishing
Journal of Physics: Condensed Matter
J. Phys.: Condens. Matter **36** (2024) 225301 (9pp)
https://doi.org/10.1088/1361-648X/ad2886

Mechanical properties of bilayer WS_2 and Graphene-WS_2 Hybrid composites by molecular dynamics simulations

Fan Wu[1,2], Huifeng Tan[1], Maurizia Palummo[2] and Luca Camilli[2,*]

[1] Center for Composite Materials and Structures, Harbin Institute of Technology, Harbin 150080, People's Republic of China
[2] Dipartimento di Fisica, Università degli studi di Roma Tor Vergata, via della Ricerca Scientifica 1, Rome, 00133, Italy

E-mail: luca.camilli@uniroma2.it

Received 13 November 2023, revised 23 January 2024
Accepted for publication 12 February 2024
Published 5 March 2024

Abstract

In the present work, by using molecular dynamics (MD) simulations, we investigate the mechanical properties of different nanostructures that may be core elements in next generation flexible/wearable photovoltaic devices, namely double layer WS_2 nanosheets (DLNS), graphene/WS_2 (layer) composites and graphene/WS_2 nanotube (NT) composites. Our results reveal that the mechanical properties of DLNS deteriorate when compared to those of monolayer WS_2. Owing to graphene's reinforcement action, the mechanical properties of graphene/WS_2 (layer) composite with both layers deformed are superior than those of WS_2, even though inferior than those of bare graphene. If stress is applied only to the graphene layer, the graphene/WS_2 composite retains the most of the strength and toughness of monolayer graphene, decreasing the fracture strength and Young's modulus by only 9.7% and 16.3%, respectively. Similarly, in the case of the graphene/WS_2 NT composite the mechanical strength and toughness experience a reduction compared to monolayer graphene, specifically by 15% and 53% for fracture strength and Young's modulus, respectively. Considering the market's keen interest in nanomaterials, particularly van der Waals (vdW) ones, for flexible and wearable photovoltaic devices, the findings presented here will significantly enhance the effective utilization of vdW composites.

Supplementary material for this article is available online

Keywords: 2D materials, grapheme, sulfer tungsten, mechanical properties, molecular dynamics simulations

* Author to whom any correspondence should be addressed.

1. Introduction

Global energy demand has experienced exponential growth in recent decades, primarily driven by population expansion and technological advancements [1, 2]. In this context, the imperative arises to discover and cultivate innovative energy solutions, with a particular emphasis on clean and renewable sources.

Photovoltaics, in which solar energy is converted into electricity [3, 4], is one form of such renewable energy. Moreover, as we are more and more dependent on portable electronic gadgets (such as smartphones, laptops and similar) that we bring with us everywhere, it would be highly beneficial to realize photovoltaic solar cell devices that are ultra-light—thus portable—flexible or even wearable.

Two-dimensional materials, in particular semiconducting transition-metal dichalcogenides (TMDs), have been recently attracting a lot of attention because of their elevated optical absorption coefficient, a range of desirable band gaps (between 1 and 2 eV) and remarkable mechanical properties [5–8] that make them promising candidates as key elements in ultra-thin and flexible/wearable photovoltaic devices [9]. Among TMDs, tungsten disulfide (WS_2) is of notable interest. First of all, it has a band gap around 2 eV that is indirect in the bulk and becomes direct at the monolayer limit [5]. It has good mechanical properties and excellent electronic and optoelectronic properties [10], such as the extremely high room-temperature mobility up to 1103 $cm^2V^{-1}S^{-1}$ [11], remarkable electrostatic coupling [12], and strong photoluminescence [13]. Secondly, WS_2 layers can wrap up to form tubular structures (that is, inorganic nanotubes, NTs) [14, 15] that have shown outstanding properties, including enhanced bulk photovoltaic effect [16].

On the other hand, among the two-dimensional materials, graphene has been suggested as the ideal transparent conductive electrode for photovoltaic devices [17] owing to its transparency, highly carrier conductivity and its impermeability, which makes it an excellent barrier coating to prevent oxidation or corrosion of more air-sensitive elements [18, 19]. More importantly, its excellent mechanical properties make graphene especially adapt for integration in ultra-thin and flexible/wearable solar cells [20–22]. Combining WS_2 with graphene as a composite is attracting interest both at experimental and theoretical/ computational level. For example, Shanmugam *et al* [23] investigated the graphene/WS_2 Schottky barrier solar cell, by using WS_2 as a photoactive layer and has a photoelectric conversion efficiency of about 3.3%. Georgiou *et al* [24] have reported a graphene vertical field-effect transistor with WS_2 layers acting as a barrier. However, for multilayer materials, the mechanical properties seem to degrade with respect to monolayer ones. It is found for bilayer graphene that interlayer dislocation between layers weakens strain transferring efficiency between the top and bottom layers [25]. Similar features have been investigated in MoS2/graphene composite, highlighting that lattice mismatch between layers will lead to a spontaneous strain energy in the interface resulting in the decreasing mechanical properties with respect to those of bare graphene [26]. Even in the case of a composite with WS2 and graphene, the mechanical properties, which are essential for optical applications, seem to degrade dramatically with respect to those of bare graphene [27].

Therefore, in the present work, we perform an extensive investigation of the mechanical properties of different nanostructures that may be core elements in next generation flexible/wearable photovoltaic devices, namely double layer WS_2 nanosheets (DLNS), graphene/WS_2 (layer) composites and graphene/WS_2 NT composites by molecular dynamics (MD) simulations. Our results reveal that the mechanical properties of DLNS deteriorate when compared to those of monolayer WS_2. Concerning the graphene/ WS_2 (layer) composite, we have considered also the case where the tensile stress is applied to either only graphene or to both graphene and WS_2. The mechanical properties of composite with both layers deformed improves with respect to WS2 but degrades with respect to graphene. Given the interest of the market in nanomaterials and especially van der Waals (vdW) materials for flexible/wearable photovoltaic devices, the results presented here will contribute to allow an efficient utilization for vdW composites.

2. Methodology

In this work, MD simulations are performed for calculating the tensile properties using the Large-scale Atomic/Molecular Massively Parallel Simulator (LAMMPS) package [28]. Bilayer nanosheets of *h*-WS_2 have been vertically arranged with the same unit cell. The monolayer WS_2 is described by pairwise (W−S, W−W, and S−S) and angle-bending (S−W−S and W−S−W) interatomic interactions. Atomic interactions are described by the Stillinger−Weber (SW) potentials [29, 30]. The fitted SW parameters [31] for monolayer WS_2 in LAMMPS are reported in table 1 of Supplemental Material. The interlayer vdW interaction between WS_2 nanosheets are defined by 12–6 Lennard Jones (LJ) potential [32] with a cut off distance of 10.0 Å that can be expressed as,

$$E^{LJ}(r_{ij}) = 4\varepsilon\left[\left(\frac{\sigma}{r_{ij}}\right)^{12} - \left(\frac{\sigma}{r_{ij}}\right)^{6}\right] \quad (1)$$

where, r_{ij} is the distance between atoms *i* and *j*, ε and σ are the energy and distance parameters, which are 0.0075 eV/3.56 Å for S–S, 0.00291 eV/3.90 Å for S–W and 0.0082 eV/3.14 Å for W–W, respectively [27].

AIREBO potential [33] is used to define the intralayer atomic interactions between C–C atoms in graphene with a covalent-bonding cutoff of 2.0 Å [34]. The interlayer vdW interaction between graphene and WS_2 is defined by LJ potential with a cut off distance of 10.0 Å, with $\varepsilon_{C\text{-}W} = 0.0036$ eV, $\sigma_{C\text{-}C}$ =3.4 Å, $\varepsilon_{C\text{-}S}$ =0.0082 eV and $\sigma_{C\text{-}S}$ =3.9 Å [27]. The uniaxial tensile simulation tests are performed by applying periodic boundary conditions to the in-plane (*x* and *y*) directions

and a free boundary condition to the out-of-plane (z) direction. The conjugate gradient scheme is used to conduct structural stabilization through energy minimization. To remove any residual stress inside the layers, the structure is then relaxed using an NVE ensemble for 50 ps and an NPT ensemble for 100 ps at atmospheric pressure and target temperature (10 K unless otherwise specified in the text), respectively, to attain their equilibrium state. Deformation is achieved by changing the size of the simulation box in the tension direction with a constant strain rate of 0.001 ps^{-1}. The tension simulation stops until the engineering strain reaches 0.3.

For choosing only one layer to be deformed, the atoms of bottom layer are selected as a group covered by using a lower square box since the two layers are set at a distance ∼5 Å.

3. Results and discussion

A uniaxial tensile analysis is performed on WS_2 DLNS with cell's size of 47.3 Å *81.9 Å. Two different conditions are considered, where either only one (DLNS-1) or two layers (DLNS-2) are stretched. For comparison, the single layer nanosheet (SLNS) with the same size is also considered. The uniaxial stretching is carried out along either the zigzag (ZZ) or armchair (AC) direction. The corresponding stress−strain curves are plotted in figure 1(a). The corresponding Young's modulus are obtained and displayed in figure 1(b), as well as the ultimate fracture stress. For SLNS along ZZ direction, the Young's modulus, fracture stress and fracture strain are 387 GPa, 72.3 GPa and 0.287, respectively, which are higher than those found for DLNS shown in figure 1(b). In uniaxial tensile deformation, as the applied strain increases, the relationship between stress and strain gradually becomes nonlinear until ultimate fracture stress is reached, followed by a sharp drop in stress typical of brittle-type failure.

Apparently, the interlayer interaction degrades the mechanical performance of DLNS along both directions. As suggested by Falin and coauthors in [33] this is possibly due to the strong directional interlayer coupling in addition to the vdW interaction, arising from electronegativity and electronic interactions of S, leading to a sliding tendency of bilayer nanosheets. Since the sliding leads to strain concentration and generally decreases the mechanical properties, the sliding tendencies in WS_2 can explain its drop in Young's modulus and fracture strength with increased layer number. It can be seen that DLNS with one layer stretched (DLNS-1) shows superior mechanical property with respect to that of DLNS with both layers stretched (DLNS-2) along both ZZ and AC directions. For tensile strain along ZZ direction, the interaction between the layers shows important influence on the mechanical behaviors, leading to the fracture stress and fracture strain in a reduced order of SLNS, DLNS-1 then DLNS-2. This tendency is comparable to previous literature [35], which investigated the mechanical properties of WS_2/WSe_2 heterostructure nanosheets with various layers by using nano indentation and DFT simulations and found a degradation of the mechanical properties with the increased layer number as due to interlayer sliding. Indeed, compared to the relaxed top nanosheet in DLNS-1, the top nanosheet in DLNS-2 is deformed as well as the bottom nanosheet, which means there are stronger interatomic interactions between layers leading to a negative effect on the mechanical performance. Similar trend has been observed when loading along the AC direction (figure 1). Indeed, fracture stress and Young's modulus of DLNS-2 slightly decreases once again indicating a degradation of the overall mechanical properties in multilayered vdW materials compared to their monolayer counterpart.

The maximum stress and its corresponding strain along the ZZ direction are higher than that along the AC direction for both DLNS-1 and DLNS-2. Stretching of DLNS along AC direction directly elongates the W–S bonds, which lay parallel to the direction of applied stress; on the other hand, in the case of stretching along the ZZ direction, the W–S bonds form a certain angle with respect to direction of applied stress so that the actual bond length deformation is reduced approximately by a factor sin30°. It is worth mentioning that other TMD materials like MoS_2 [36], $MoSe_2$ [37], and WSe_2 [38] also show similar characteristics of being more resilient to fracture under ZZ rather than AC loading, which in fact happens for monolayer graphene as well [39, 40].

To unveil the failure mechanism, the atomic von Mises stress [41] distribution of DLNS-2 during the tensile process along AC and ZZ directions, is estimated and reported in figures 1(c) and (d). As the induced deformation continues, the stress distributions tend to be different along ZZ and AC direction. For ZZ direction, it can be clearly seen that the nanosheets are deformed steadily with stress evenly distributed over the nanosheets leading to a relatively high fracture strain. In contrast, in the case of deformation along AC direction, the DLNS-2 develops stress concentration, as it is observed in figure 1(d). Notably, the stress is concentrated in the middle area of the nanosheet during loading along the AC direction. As a result of such stress concentration, the nanosheets tend to break down more easily. Furthermore, it is found that only one of the two layers fractures when the DLNS-2 breaks down along the AC direction. An uneven stress distribution also takes place between the two nanosheets with one layer undertaking the majority stress during the tensile process. The DLNS-1 with various surface ratios (0.2, 0.4, 0.6, 0.8) between the 2 layers are investigated in figure S1. The ratios influence only slightly the mechanical performance of DLNS-1.

To understand the mechanical properties of the hybrid graphene and WS_2 composite, we first consider the case with both graphene and WS_2 nanosheet (GWSB) being deformed along ZZ or AC direction. Figure 2(a) displays the configuration of GWSB after energy minimization. To comparatively analyze the effects of vdW interaction on GWSB and its mechanical behavior, bare graphene and bare WS_2 nanosheet are also simulated, as shown in figure 2(b). Different from the smooth curves of monolayer graphene, the stress–strain curves of GWSB are similar to those found for WS_2 nanosheet with a lower fracture stress than graphene. There is also a distinct

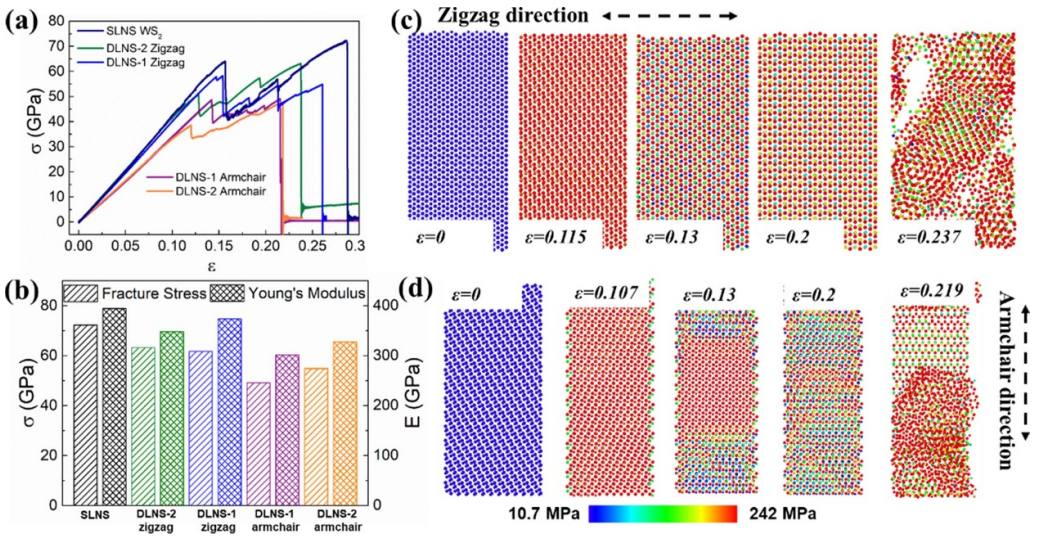

Figure 1. (a) The stress (σ) -strain (ε) curves of SLNS and DLNS with either one layer stretched or both layers stretched in ZZ and AC chirality. (b) The comparisons of fracture (σ_f) stress and Young's modulus (E) for SLNS and DLNSs. (c), (d) Mises stress distribution for the case of DLNS-2, at sequential strain during stretching along ZZ and (d) AC direction.

difference with respect to chirality, along the zig-zag (GWSB-ZZ) and armchair (GWSB-AC) direction. It can be seen that, in both cases, GWSB shows elastic deformation at the early stage of tensile loading. Afterward, the situation changes for GWSB-ZZ or GWSB-AC. In the case of GWSB-ZZ, the stress continues to achieve the final fracture point after a slightly shaking or sliding between the layers. On the other hand, the stress of GWSB-AC increases non-linearly with increasing strain up to ultimate tensile strength (P_c), followed by a sharp drop in stress which corresponds to the brittle-type failure of individual layers. The stress at final fracture strain (P_f) is lower than that at P_c, which is distinctive from the others. The detailed movements of GWSB during the deformation are illustrated in figures 2(c) and (d).

As shown in figures 2(c) and (d), the GWSB-AC is deformed gradually until strain of 0.146, (P_c). It can be seen from the snapshots at different strain values that the stress in the whole structure is distributed uniformly before P_c. However, after the step-like jump fracture at P_c, the monolayer graphene is broken with the WS_2 nanosheet taking the remaining deformation. Thus, interestingly, it is the graphene that fractures first. In the simulation, graphene and WS_2 are instantaneously deformed with same strain. For graphene, there are six load-bearing bonds per unit cell located at one layer. On the other hand, WS_2 sheet consists of a layer of tungsten atoms sandwiched between two layers of sulfur atoms forming a trigonal prismatic crystal system. The constituent bond angles in WS_2 can expand more under loading as compared to the graphene along AC direction, which reasonably explains our findings.

Hence, the fracture strain and fracture stress for GWSB-AC are 0.146 and 99.6 MPa respectively as shown at P_c. In contrast, GWSB-ZZ is deformed gradually, with stress distributed evenly in two layers, until final fracture is achieved. As a result, the fracture strain is higher than in the case of GWSB-AC. Still, it is found that fracture strain of GWSB along the AC direction is larger than that of bare graphene and smaller than bare WS_2. It can be found that the fracture strain is not related to the intrinsic performance of WS_2 since fracture initiates from the graphene layer. This reduction or increment in fracture strain of the GWSB when compared to the monolayer graphene and WS_2, respectively, is consistent with previous literature on this [27] and other heterostructure systems [42].

For detailed comparison among GWSB, monolayer graphene and WS_2 nanosheet, the fracture strain and fracture stress are reported in table 1 with Young's modulus. It can be seen that, for ZZ loading, monolayer graphene exhibits significantly greater fracture stress and fracture strain than AC loading. Subsequently, Young's modulus is comparatively higher in AC loading than ZZ loading. Similarly, the WS_2-ZZ shows higher fracture stress and fracture strain than WS_2-AC, with almost the same Young's modulus. As for GWSB, the critical point P_c and P_f in GWSB-AC are both presented for a clear view. It can be seen that GWSB-ZZ and GWSB-AC possess almost same ultimate fracture stress and Young's modulus, which are both increased compared to WS2 nanosheet. The fracture stress increased from 48 MPa to 97 MPa along AC direction, whereas increased from 72 MPa to 102 MPa along ZZ direction. GWSB-ZZ has a lower fracture strain compared to the monolayer graphene and monolayer WS_2 for ZZ loading. A noteworthy observation is that the fracture strain of GWSB-AC is hard to be defined. According to the step-jump fracture and lower stress at final fracture in figure 2(b), there may be an individual layer breakdown at P_c. Since the failure of any layer corresponds to the failure of the composite of GWSB-AC. Compared with other work at

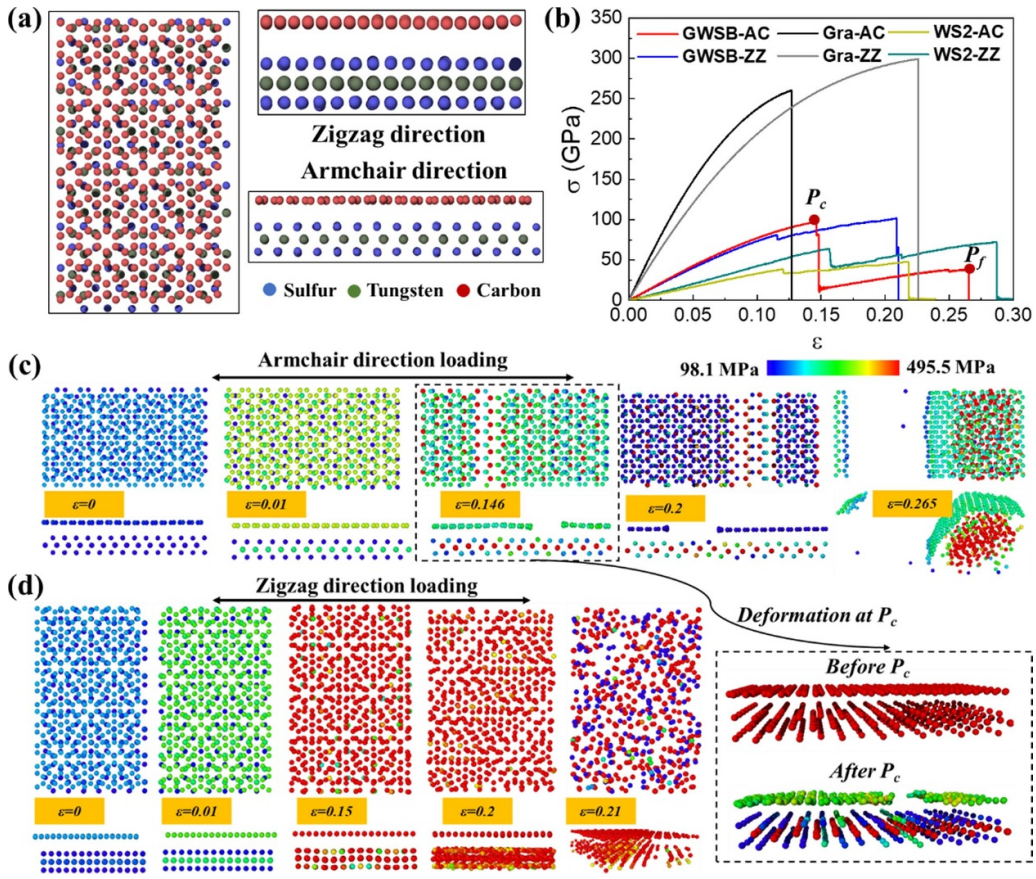

Figure 2. (a) Configuration of GWSB with both layers being stretched in periodic boundary along ZZ and AC direction. (b) The stress–strain curves of GWSB compared with those of individual graphene and WS_2 nanosheet. (c), (d) The Mises stress distribution of GWSB during tensile deformation along AC and ZZ direction.

Table 1. Comparison of ultimate stress, fracture strains and Young's Modulus of the GWSB, monolayer graphene and WS_2 nanosheet.

	Armchair direction			Zigzag direction		
Materials	Fracture stress (GPa)	Fracture strain	Young's modulus (GPa)	Fracture stress (GPa)	Fracture strain	Young's modulus (GPa)
GWSB	97.11 (P_c) 38.5 (P_f)	0.146 (P_c) 0.265 (P_f)	866.2	101.63	0.21	807.7
Graphene	260.24	0.126	3342	299.04	0.225	2704
WS_2	47.6	0.218	326.8	72.25	0.287	371.4

300 K, the temperature plays an important role on the mechanical properties of monolayer graphene and WS_2 nanosheet at ZZ and AC directions. But the fracture stress and Young's modulus show a similar trend at ZZ and AC directions.

Since from a practical point of view the role of temperature is clearly very important, we have performed MD simulations at different temperatures. Figure 3(a) shows the stress–strain curves of GWSB along ZZ and AC deformation at 10 K and 300 K. It can be seen that there are similar step-jump features associated to sharp fracture that occurred in GWSB-AC at both 10 K and 300 K, as also shown in left zoom-in picture. The sharp jumps in the curves of GWSB-AC corresponds to fracture of graphene layer, thus of the whole composite. At both temperatures, the fracture stress and fracture strain of GWSB-ZZ are higher than that of GWSB-AC, as expected [27]. For GWSB-ZZ, from 10 K to 300 K, the fracture stress decreases from 101.7 MPa to 91.82 MPa, that is by 9.7%, while the fracture strain decreases from 0.21 to 0.17, that is by 19%. It can be seen from the zoom-in at right in figure 3(a) that the latter deformation of GWSB-ZZ tends to be rough and unstable at 300 K. On the other hand, the fracture stress and fracture strain of GWSB-AC from 10 K to 300 K reduce from 97.27 MPa to 77 MPa, that is by 20.8%, and from 0.146 to 0.118, that is by 19.2%, respectively. The corresponding Young's modules are not presented as an individual figure since there is less than 4% variation among them. Therefore, one can notice

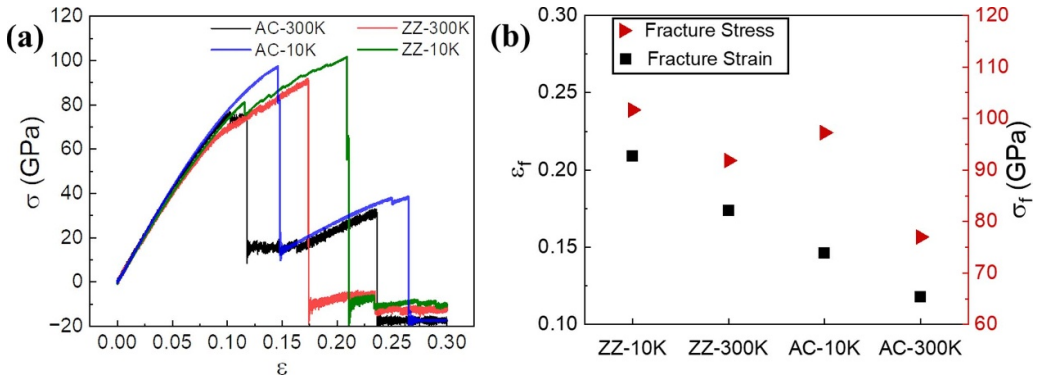

Figure 3. (a) Stress–strain curves of GWSB along ZZ and AC direction at temperature of 10 K and 300 K. (b) The fracture stress with corresponding strain of GWSB along ZZ and AC direction at temperature of 10 K and 300 K.

that as temperature increases, the mechanical performance of the composite weakens regardless of chirality. Yet, the effect of temperature is somewhat more significant and evident on the mechanical performance of GWSB-AC compared to GWSB-ZZ.

In the next simulation, the composite is deformed with stress applied to only graphene (GWS) along ZZ or AC direction in order to obtain a better understanding of the mechanism underpinning mechanical failure of the composite. Figure 4(a) displays the structural configuration used in the simulation, with a size of 66.5 Å * 85.5 Å. The top WS_2 layer is arranged on top of graphene. Furthermore, in this study both chirality and the ratio between the layers in the composite are considered during deformation, as shown in figures 4(b) and (c). Concerning chirality, there are four combinations, namely graphene ZZ/WS_2 ZZ (GWS-ZZZZ), graphene ZZ/WS_2 AC (GWS-ZZAC), graphene AC/WS_2 AC (GWS-ACAC) and graphene AC/WS_2 ZZ (GWS-ACZZ). As shown in figure 4(b), these four cases are divided into two groups classified by the chirality of graphene. As mentioned above, the vdW interaction between layers as well as chirality of layers both play crucial roles in determining the mechanical performance of DLNS-1 for WS_2 nanosheets. However, it is noticeable for GWS composites with graphene in ZZ direction (that is, both GWS-ZZZZ and GWS-ZZAC) that the mechanical performances are very similar to those of bare graphene. In other words, regardless of the chirality of WS_2 nanosheet, the presence of WS_2 in the composite basically has no effect on the overall mechanical properties when stress is applied only to graphene. Somewhat similar phenomena are observed for GWS-ACAC and GWS-ACZZ, even though in these cases adding the WS_2 nanosheets seems to have a slight negative influence on the mechanical performance of the composite compared to those of bare graphene. Specifically, compared with bare graphene stretched along the AC direction, the fracture stress of GWS-ACAC and GWS-ACZZ decrease slightly from 251 GPa to 242 GPa, that is by 3.5%, with an increased fracture strain from 0.125 to 0.142, that is by 13.6%.

It is known that graphene exhibits significantly higher mechanical properties than WS_2 nanosheets [18, 31], which explains why the graphene/WS_2 nanosheet composite has reduced mechanical properties compared to graphene. Furthermore, graphene displays higher fracture stress and strain along ZZ direction than that along AC direction [39]. It can be concluded that since graphene along ZZ direction is stiffer and tougher than along AC direction, this may in turn results in the negligible influence by WS_2 nanosheet.

Concerning the ratio between the WS_2 nanosheet and graphene, as reported in figure 4(c), it has no effect on the mechanical properties of GWS. A similar comment can be done for the chirality of WS_2. From the Mises distribution of GWS-ACAC in figure 4(d) it can be seen that the graphene undertakes the majority of the stress during the tensile process with WS_2 nanosheet being relaxed and sliding back and forth. It is also consistent with DLNS-1 that only the boundary of the top layer is affected in a slight way by the tensile deformation of the graphene.

We have expanded our investigation on the mechanical properties of graphene and WS_2 hybrid composite by considering also a WS_2 nanotube on top of graphene (GNT) with only graphene layer being deformed. This is performed to reproduce a scenario where a film of WS_2 NTs is deposited on a graphene sheet the size of which is considerably larger than that of an individual NT. In this case, if a stress is applied to the composite, this will be applied to graphene's ends. The GNT composite is modeled with a WS_2 nanotube with outer diameter of 46.7 Å and length of 66.8 Å on top of the graphene nanosheet with size 212.5 Å * 246.2 Å. For comparison, the mechanical properties of an isolated WS_2 nanotube are shown in figure S2. Figures 5(c) and (d) show the initial steps during deformation and the stress–strain curves of GNT compared with that of bare graphene. When GNT is deformed along the axial direction of the WS_2 nanotube, the graphene tends to gradually wrap around the nanotube. Then, the graphene is stretched as a 'graphene-tube' until final fracture. Interestingly, when the stress is applied perpendicularly to the WS_2 nanotube axis, the nanotube rotates until its axis lies parallel to the deforming direction. At that point, the situation is similar to the previously analyzed case. Figure S3 displays the mechanical property of GNT with different nanotube lengths. Increased nanotube length leads to decreased fracture stress. The corresponding stress–strain results are plotted in figure 5(b) compared with other TMD/graphene in literatures [27, 42]. The WS_2/graphene/WS_2 sandwich composite and

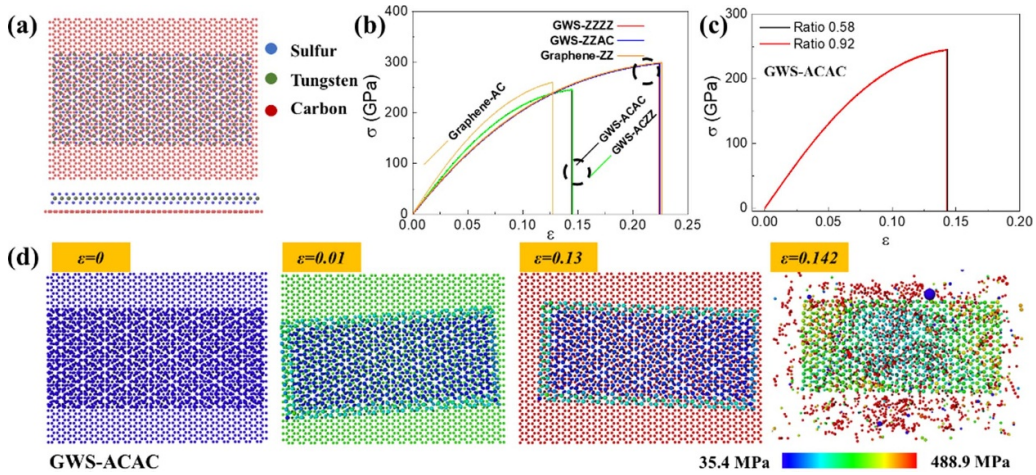

Figure 4. (a) Configuration of the composite combing graphene and WS_2 nanosheet (GWS). (b) Stress–strain curves of GWS with graphene stretched along different chiral directions. (c) Stress–strain curves of GWS with different ratios between WS_2 (AC) and graphene (AC). (d) The Mises stress distribution of GWS with ratio 0.58 between WS_2 (AC) and graphene (AC) during tensile deformation.

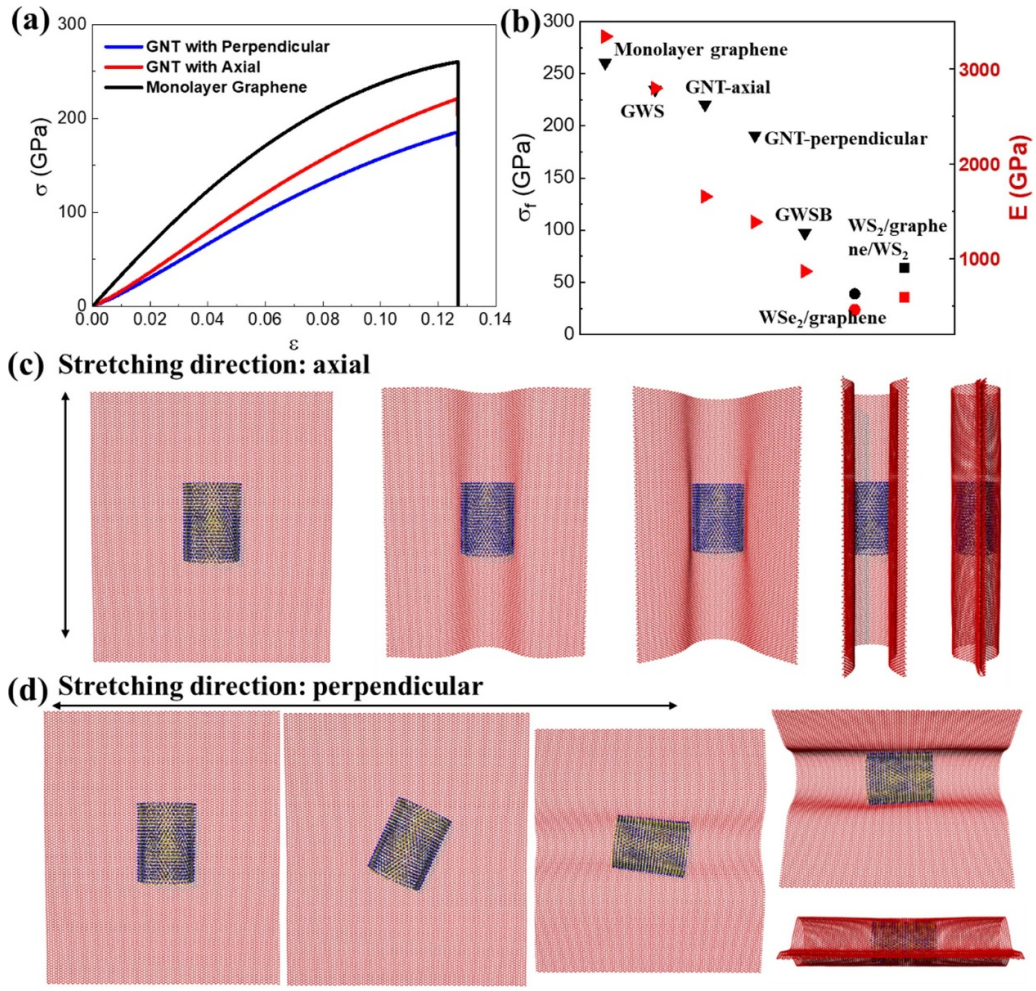

Figure 5. (a) The corresponding stress–strain curves compared with monolayer graphene. (b) the comparison of fracture stress (black symbols) and Young's modulus (red symbols) of this work (GNT, GWS and GWSB) and other literatures (last two in square symbols and circle symbols, respectively). (c) The snapshots at the initial steps of graphene and WS_2 nanotube composite (GNT) with graphene deformed along nanotube axial direction. (d) The snapshots at the initial steps of graphene and WS_2 nanotube composite (GNT) with graphene deformed in the direction perpendicular to nanotube axial direction.

WSe_2/graphene heterostructure are both deformed with all layers showing a dramatically decreased fracture stress and Young's modulus with respect to monolayer graphene. As for GNT, fracture stress and Young's modulus along either direction decrease compared to monolayer graphene. Moreover, the fracture stress and Young's modulus of GNT-perpendicular are reduced compared to those of GNT-axial. It is suggested that the sliding between graphene and WS_2 nanotube has a significant effect on the mechanical performance of graphene which is similar to the GWS. However, it works in different ways. When it comes to GNT-perpendicular, it can be clearly seen that the initial rotation of WS_2 nanotube enhances the interaction between them by increasing the wrapping time and expanding the interaction surface. As a result, the improved interactions between the layers weaken the mechanical performance of GNT compared with GWS in both fracture stress (σ_f) and Young's modulus (E). The composite of graphene and WS_2 nanosheet shows a better mechanical performance with respect to graphene and WS_2 nanotube composite with only graphene deformed.

4. Conclusion

We investigated the mechanical properties of different nanostructures that may be core elements in next generation flexible/wearable photovoltaic devices, namely bilayer WS_2 nanosheets (DLNS), graphene/WS_2 (layer) composites and graphene/WS_2 NT composites by MD simulations. Our results reveal that the mechanical properties of DLNS deteriorate when compared to those of monolayer WS_2. This was found for the case of either only one or both layers being subject to tensile stress. The mechanical properties of graphene/WS_2 (layer) composite with both layers deformed improved with respect to bare WS_2 but degraded with respect to bare graphene. Interestingly, it is graphene that fractures first in the composite. Temperature also plays an essential role as higher temperatures weaken the composite's toughness and strength. However, the graphene/WS_2 (layer) composite retains most of its strength and toughness of monolayer graphene when tensile stress applied to only graphene, with a decrease by only 9.7% and 16.3% for fracture strength and Young's modulus, respectively. Also, our findings on graphene/WS_2 NT reports a slightly reduced mechanical strength and toughness with respect to monolayer graphene by 15% and 53%, for fracture strength and Young's modulus, respectively. In conclusions, our investigation of the mechanical properties and failure mechanism for bilayer nanosheet and composites between graphene and WS_2 nanostructures may be very useful for their practical applications in future flexible or wearable electronic and opto-electronic devices [43–45].

Data availability statement

The data cannot be made publicly available upon publication because they are not available in a format that is sufficiently accessible or reusable by other researchers. The data that support the findings of this study are available upon reasonable request from the authors.

Acknowledgments

This research was in part sponsored by the NATO Science for Peace and Security Program under Grant id. G5936.

ORCID iD

Luca Camilli https://orcid.org/0000-0003-2498-0210

References

[1] Grubler A *et al* 2018 *Nat. Energy* **3** 515
[2] Ahmad T and Zhang D 2020 *Energy Rep.* **6** 1973
[3] Wang W *et al* 2019 *Nat. Commun.* **10** 3012
[4] Hernández-Callejo L, Gallardo-Saavedra S and Alonso-Gómez V 2019 *Sol. Energy* **188** 426
[5] Li Q, Rao H, Yang X, Guo Z, Gong W, Ma X and Li B 2022 *J. Phys. Chem.* C **126** 9293
[6] Rakita O A, Nikolić N, Mildner M, Matiasek J and Elbe-Bürger A 2020 *Sci. Rep.* **10** 1
[7] Shi J *et al* 2016 *Adv. Mater.* **28** 10664
[8] Bin Rafiq M K S, Amin N, Alharbi H F, Luqman M, Ayob A, Alharthi Y S, Alharthi N H, Bais B and Akhtaruzzaman M 2020 *Sci. Rep.* **10** 1
[9] Nassiri Nazif K *et al* 2021 *Nat. Commun.* **12** 1
[10] Lan C, Li C, Ho J C and Liu Y 2021 *Adv. Electron. Mater.* **7** 1
[11] Zhang W, Huang Z, Zhang W and Li Y 2014 *Nano Res.* **7** 1731
[12] Braga D, Gutiérrez Lezama I, Berger H and Morpurgo A F 2012 *Nano Lett.* **12** 5218
[13] Weijie Z, Zohreh G, Leiqiang C, Minglin T, Christian K, PingHeng T and Goki E 2013 *ACS Nano* **7** 791
[14] Manashi N, Achutharao G and Rao R C N 2001 *Adv. Mater.* **13** 283
[15] Rothschild A, Sloan J and Tenne R 2000 *J. Am. Chem. Soc.* **122** 5169
[16] Zhang Y J, Ideue T, Onga M, Qin F, Suzuki R, Zak A, Tenne R, Smet J H and Iwasa Y 2019 *Nature* **570** 349
[17] Mahmoudi T, Wang Y and Hahn Y B 2018 *Nano Energy* **47** 51
[18] Bunch J S, Verbridge S S, Alden J S, Van Der Zande A M, Parpia J M, Craighead H G and McEuen P L 2008 *Nano Lett.* **8** 2458
[19] Camilli L, Yu F, Cassidy A, Hornekær L and Bøggild P 2019 *2D Mater.* **6** 022002
[20] Ruan K, Ding K, Wang Y, Diao S, Shao Z, Zhang X and Jie J 2015 *J. Mater. Chem.* A **3** 14370
[21] Yoon J, Sung H, Lee G, Cho W, Ahn N, Jung H S and Choi M 2017 *Energy Environ. Sci.* **10** 337
[22] He M, Jung J, Qiu F and Lin Z 2012 *J. Mater. Chem.* **22** 24254–64
[23] Shanmugam M, Jacobs-Gedrim R, Song E S and Yu B 2014 *Nanoscale* **6** 12682–9
[24] Georgiou T *et al* 2013 *Nat. Nanotechnol.* **8** 100–3
[25] Yang L, Xu H, Liu K, Gao D, Huang Y, Zhou Q and Wu Z 2020 *Nanotechnology* **31** 125704
[26] Jiang J W and Park H S 2014 *Appl. Phys. Lett.* **105** 033108
[27] Oishi T M T, Malakar P, Islam M and Islam M M 2021 *Comput. Condens. Matter* **29** 612
[28] Plimpton S 1994 *J. Comput. Phys.* **117** 1
[29] Jiang J-W and Zhou Y-P 2017 Parameterization of stillinger-weber potential for two-dimensional atomic crystals (IntechOpen) (https://doi.org/10.5772/intechopen.71929)

[30] Ma L, Tan Y, Ghorbani-Asl M, Boettger R, Kretschmer S, Zhou S, Huang Z, Krasheninnikov A V and Chen F 2017 *Nanoscale* **9** 11027
[31] Tang H, Hu D, Cui Z, Ye H and Zhang G 2021 *J. Phys. Chem.* C **125** 2680
[32] Devonshire A F 1938 *Nature* **141** 1148
[33] Stuart S J, Tutein A B and Harrison J A 2000 *J. Chem. Phys.* **112** 6472
[34] Dewapriya M A N, Srikantha Phani A and Rajapakse R K N D 2013 *Model. Simul. Mater. Sci.* **21** 065017
[35] Falin A *et al* 2021 *ACS Nano* **15** 2600
[36] Jiang J W, Park H S and Rabczuk T 2013 *J. Appl. Phys.* **114** 064307
[37] Wang X, Hong Y, Wang M, Xin G, Yue Y and Zhang J 2019 *Phys. Chem. Chem. Phys.* **21** 9159
[38] Wenyang D, Dan H, Jingchao Z and Xinyu W 2019 *Mater. Res. Express* **6** 085071
[39] Zhang Y Y, Pei Q X and Wang C M 2012 *Appl. Phys. Lett.* **101** 081909
[40] Zhao H, Min K and Aluru N R 2009 *Nano Lett.* **9** 3012
[41] Barsanescu P D and Comanici A M 2017 *Acta Mech.* **228** 433–46
[42] Chowdhury E H, Rahman M H, Fatema S and Islam M M 2021 *Comput. Mater. Sci.* **188** 110231
[43] Britnell L *et al* 2013 *Science* **340** 1311–4
[44] Yeh C-H, Liang Z-Y, Lin Y-C, Ma C-H, Chu Y-H, Suenaga K and Chiu P-W 2020 *ACS Appl. Electron. Mater.* **2** 3898–905
[45] Yeh C-H, Chen H-C, Lin H-C, Lin Y-C, Liang Z-Y, Chou M-Y, Suenaga K and Chiu P-W 2019 *ACS Nano* **13** 3269–79